

## **Grid-Current-Feedback Active Damping for LCL Resonance in Grid-Connected Voltage-Source Converters**

Wang, Xiongfei; Blaabjerg, Frede; Loh, Poh Chiang

*Published in:*  
I E E E Transactions on Power Electronics

*DOI (link to publication from Publisher):*  
[10.1109/TPEL.2015.2411851](https://doi.org/10.1109/TPEL.2015.2411851)

*Publication date:*  
2016

*Document Version*  
Early version, also known as pre-print

[Link to publication from Aalborg University](#)

*Citation for published version (APA):*  
Wang, X., Blaabjerg, F., & Loh, P. C. (2016). Grid-Current-Feedback Active Damping for LCL Resonance in Grid-Connected Voltage-Source Converters. *I E E E Transactions on Power Electronics*, 31(1), 213-223.  
<https://doi.org/10.1109/TPEL.2015.2411851>

### **General rights**

Copyright and moral rights for the publications made accessible in the public portal are retained by the authors and/or other copyright owners and it is a condition of accessing publications that users recognise and abide by the legal requirements associated with these rights.

- Users may download and print one copy of any publication from the public portal for the purpose of private study or research.
- You may not further distribute the material or use it for any profit-making activity or commercial gain
- You may freely distribute the URL identifying the publication in the public portal -

### **Take down policy**

If you believe that this document breaches copyright please contact us at [vbn@aub.aau.dk](mailto:vbn@aub.aau.dk) providing details, and we will remove access to the work immediately and investigate your claim.



# Grid-Current-Feedback Active Damping for *LCL* Resonance in Grid-Connected Voltage Source Converters

Xiongfei Wang, *Member IEEE*, Frede Blaabjerg, *Fellow IEEE*, and Poh Chiang Loh

**Abstract**—This paper investigates active damping of *LCL*-filter resonance in a grid-connected voltage source converter with only grid-current feedback control. Basic analysis in the *s*-domain shows that the proposed damping technique with a negative high-pass filter along its damping path is equivalent to adding a virtual impedance across the grid-side inductance. This added impedance is more precisely represented by a series *RL* branch in parallel with a negative inductance. The negative inductance helps to mitigate phase lag caused by time delays found in a digitally controlled system. The mitigation of phase-lag, in turn, helps to shrink the region of non-minimum-phase behavior caused by negative virtual resistance inserted unintentionally by most digitally implemented active damping techniques. The presented high-pass-filtered active damping technique with a single grid-current feedback loop is thus a more effective technique, whose systematic design in the *z*-domain has been developed in the paper. For verification, experimental testing has been performed with results obtained matching the theoretical expectations closely.

**Index Terms**—Voltage source converter, *LCL* filter, resonance damping, non-minimum phase system, virtual impedance

## I. INTRODUCTION

*LCL* resonance has always been an important concern for *LCL*-filtered voltage source converters [1]. A wide variety of resonance damping techniques have thus been developed with the trend generally favoring active damping techniques because of the additional power losses experienced by passive damping techniques [2]. Active damping techniques can also be broadly divided into those realized by cascading a digital filter with the current controller [3], and those realized by feeding back the filter state variables [4]–[16]. The former represents a sensor-less technique realized by plugging in a digital filter, which unfortunately, is sensitive to parameter uncertainties and variations [10]. It is therefore not as popular as the feedback of filter state variables for damping purposes. Among the state variables fed back, the filter capacitor current has been widely chosen [4]–[9], and is usually realized with a proportional resistive gain.

The proportional resistive gain is, however, easily modified by transport delays found in a digital system. The outcome is a negative virtual resistance, which upon introduced, will add open-loop Right-Half-Plane (RHP) poles to the system. These open-loop poles will, in turn, introduce a non-minimum-phase closed-loop behavior to the system [7]. Such a non-minimum-phase behavior has subsequently been resolved by replacing the usual proportional gain with a High-Pass Filter (HPF) along the capacitor current feedback loop [8]. The capacitor current must however still be measured, which in practice, will demand an additional sensor or a complex software-based observer [6].

To avoid additional sensing, the single-loop current control schemes have increasingly been studied [9]–[16]. In [11], for example, it has been shown that a stable grid current control scheme can be implemented with only a single control loop without damping. The reason has been identified as an inherent damping introduced by the transport delays in the considered digital control system. This inherent damping effect is however available only when the *LCL* resonance frequency is above one-sixth of the system sampling frequency [9], [12]. It is, therefore, not always suitable like in weak grids, where grid impedances and hence system *LCL* resonance frequencies may vary widely. As a precaution, the external active damping is recommended, especially in the power-electronics-based power systems, where the interactions among multiple converters may lead to harmonic instability if not damped appropriately [13].

It is therefore encouraging to develop a robust active damping technique that relies only on the feedback of grid-side current (hence no additional sensor) [14]–[17]. Ideally, the developed scheme will require an  $s^2$  term for inserting the necessary positive virtual resistance, which in practice, is not implementable because of the possible noise amplification. A second-order Infinite Impulse Response (IIR) filter [14] or a first-order HPF with a negated output [15], [16] has thus been suggested as a replacement for the  $s^2$  term. Another alternative is to use the optimized loop shaping design discussed in [17], where the current controller and active damping have been designed together as a fifth-order feedback transfer function in the *z*-domain. In terms of simplicity, the HPF is clearly more attractive, while not compromising accuracy significantly. Its parameter design has thus been discussed in [15] and [16], but not its alteration caused by the transport delays. Its equivalent circuit notation has also not been discussed. These issues, when

Manuscript received October 7, 2014; revised January 10, 2015; accepted March 01, 2015. This work was supported by European Research Council (ERC) under the European Union's Seventh Framework Program (FP7/2007-2013)/ERC Grant Agreement no. [321149-Harmony].

X. Wang, F. Blaabjerg, and P. C. Loh are with the Department of Energy Technology, Aalborg University, 9220 Aalborg, Denmark (e-mail: xwa@et.aau.dk, fbl@et.aau.dk, pcl@et.aau.dk).

left unresolved, will more easily lead to non-minimum-phase response of the system, owing to the overlooked presence of negative virtual resistance.

This paper thus begins by presenting an impedance-based analysis in the  $s$ -domain for generalizing the physical circuit property of grid current feedback active damping. The analysis specifically demonstrates that the grid current active damping is equivalent to the insertion of a virtual impedance in parallel with the grid-side inductance. In case of a HPF with a negated output along the damping path, the virtual impedance can further be notated as a series  $RL$  branch in parallel with a negative inductance. The resistive part of the  $RL$  branch may become negative when influenced by transport delays, which may then cause non-minimum-phase response that can impair the overall system stability and robustness. The non-minimum-phase problem can, however, be minimized by the negative virtual inductance in parallel with the series  $RL$  damper.

This mitigation effect is not inherited by other existing active damping techniques based on the feedback of filter capacitor current, and has presently not been discussed in the literature. It is thus the intention of this paper to study the combined negative resistive and inductive effects introduced by the grid current active damping. Moreover, the frequency region, within which negative virtual resistance exists, will also be identified, and shown to be dependent on the ratio between HPF cutoff frequency and system sampling frequency. A robust damping performance can subsequently be ensured by developing a systematic co-design procedure for the active damping and grid current controller. The procedure is explained with root locus analyses in the  $z$ -domain, before verifying it experimentally.

## II. IMPEDANCE-BASED ANALYSIS

### A. System Description

Fig. 1 illustrates a three-phase grid-connected voltage source converter with an  $LCL$  filter and a constant DC-link voltage  $V_{dc}$  for simplicity. Parasitic resistances of the circuit have been ignored to arrive at the worst case condition, where no passive damping of resonance exists. The Synchronous Reference Frame Phase-Locked Loop (SRF-PLL) has also been employed for synchronizing the converter with the Point of Common Coupling (PCC) voltage [18]. A low-bandwidth SRF-PLL has been designed to avoid the undesired low-frequency instability [19]. The grid voltage  $V_g$  has also been assumed as balanced, which then allows per-phase diagrams to be used for analysis in Fig. 2, where the per-phase grid current control scheme has been shown. The illustrated scheme clearly has the grid current  $i_2$  sensed and fed back for regulation and active damping purposes. For current regulation, controller  $G_c(s)$  used is the Proportional-Resonant (PR) controller represented by (1) in the stationary  $\alpha\beta$  frame [9].

$$G_c(s) = k_p + \frac{k_i s}{s^2 + \omega_1^2} \quad (1)$$

where  $k_p$  and  $k_i$  are proportional and resonant gains, respectively, and  $\omega_1$  is the grid fundamental frequency.

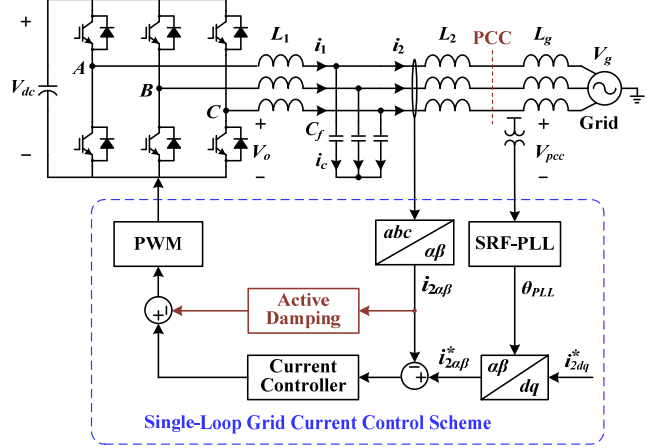


Fig. 1. Three-phase grid-connected  $LCL$ -filtered voltage source converter with single-loop grid current control scheme.

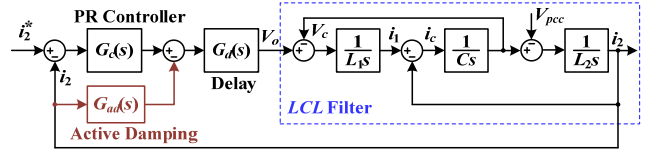


Fig. 2. Per-phase block diagram of the grid current control loop.

Complementing,  $G_{ad}(s)$  is for active damping, whose transfer function is analyzed in the following subsections. Influencing  $G_c(s)$  and  $G_{ad}(s)$  is the digital time delay  $G_d(s)$ , whose notation is given in (2) [20].

$$G_d(s) = e^{-1.5T_s s} \quad (2)$$

where  $T_s$  is the system sampling period. The digital time delay is composed by the half sampling period of modulation delay, and one sampling period of computation delay.

### B. Impedance-Based Equivalent Circuits

For demonstrating circuit properties realized by grid current active damping, its representation in Fig. 2 is redrawn as in Fig. 3 (a), after introducing the following two modifications, while keeping the system closed-loop response unchanged.

- Instead of sensing grid current  $i_2$  in Fig. 2, voltage across the grid-side inductor  $L_2$  is sensed in Fig. 3 (a).
- Instead of adding at the output of  $G_c(s)$  in Fig. 2, the summing node has been shifted to after  $1/(L_2 s)$  in Fig. 3 (a).

For retaining its closed-loop characteristics,  $Z_v(s)$  in Fig. 3 (a) is further set as (3).

$$Z_v(s) = \frac{L_1 L_2 s^2}{G_{ad}(s) G_d(s)} \quad (3)$$

Transfer functions surrounded by the dashed enclosure in Fig. 3 (a) can eventually be redrawn like the equivalent circuit shown in Fig. 3 (b). This representation immediately informs

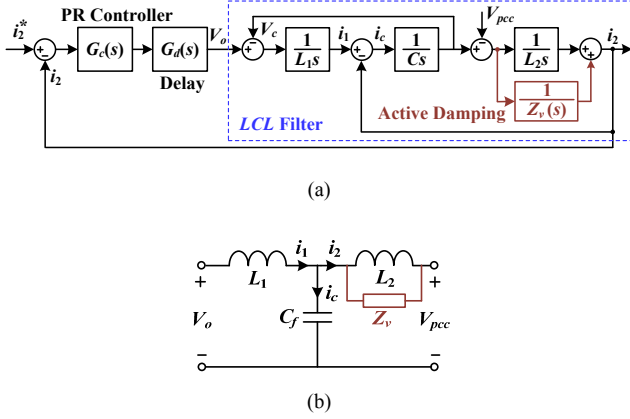


Fig. 3. Equivalent control diagram and generalized equivalent circuit for the grid current active damping scheme. (a) Control diagram. (b) Equivalent circuit.

that grid current active damping is no different from paralleling a virtual impedance  $Z_v(s)$  across the grid-side inductance  $L_2$ . The added impedance can be shaped by varying  $G_{ad}(s)$  rather than  $G_d(s)$ , which is usually fixed by the chosen sampling frequency. For example, with  $G_d(s) = 1$  fixed by having no system delay, a resistive damper  $Z_v(s) = R_v$  like in Fig. 4 (a) can be inserted by shaping  $G_{ad}(s) = s^2$  for cancelling the same  $s^2$  term found in the numerator of (3).

Shaping  $G_{ad}(s) = s^2$  is, however, not practically feasible, leading next to the series  $RL$  damper represented by (4) and shown in Fig. 4 (b). The series  $RL$  damper can be implemented by  $G_{ad,1}(s)$  in (5), which clearly does not have the undesired  $s^2$  term, yet is still having a first-order derivative term, which in practice, is commonly approximated by a first-order HPF term. That makes it no different from the second HPF term in (5).

$$Z_{v,1}(s) = L_{v,1}s + R_{v,1} \quad (4)$$

$$G_{ad,1}(s) = \frac{L_1 L_2 s^2}{L_{v,1}s + R_{v,1}} = \frac{L_1 L_2 s}{L_{v,1}} - \frac{L_1 L_2 R_{v,1} s}{L_{v,1}(L_{v,1}s + R_{v,1})} \quad (5)$$

A third possibility is thus to consider only the second HPF term in (5) with its negative polarity retained (implemented by placing a HPF with negated output along the damping path). Note that the same high-pass scheme has been mentioned in [15] and [16], yet neither its physical circuit meaning nor the accompanied nontrivial features are discussed. These issues are investigated here by deriving its circuit equivalence using the analytical technique developed earlier. Transfer functions and circuit representation obtained are shown in (6), (7) and Fig. 4 (c).

$$\begin{aligned} Z_{v,2}(s) &= \frac{-L_{v,2}s(L_{v,2}s + R_{v,2})}{R_{v,2}} \\ \Rightarrow G_{ad,2}(s) &= \frac{-L_1 L_2 R_{v,2} s}{L_{v,2}(L_{v,2}s + R_{v,2})} \end{aligned} \quad (6)$$

$$G_{ad,2}(s) = \frac{-k_{ad}s}{s + \omega_{ad}} \Rightarrow k_{ad} = \frac{L_1 L_2 R_{v,2}}{L_{v,2}^2}, \quad \omega_{ad} = \frac{R_{v,2}}{L_{v,2}} \quad (7)$$

where  $L_{v,2}$  and  $R_{v,2}$  are virtual inductance and resistance furnished by the HPF active damping, and  $\omega_{ad}$  and  $k_{ad}$  are cutoff frequency and gain of the HPF, respectively.

Fig. 4 (c) again shows a series  $RL$  damper, but now with an additional negative virtual inductance ( $-L_{v,2}$ ) connected in parallel. This negative virtual inductance, if chosen equal to the grid-side inductance  $L_2$ , will lead to only  $R_{v,2}$  and  $L_2$  in series on the grid-side of the filter. The HPF gain in (7) will also simplify to  $k_{ad} = \omega_{ad} L_1$ . However, this simplified case is only for the conceptual information, since the grid-side inductance will drift in practice, making it hard to be exactly cancelled by the negative virtual inductance in parallel.

Then, with a finite time delay considered, the virtual impedance in (4) changes to (8) and (9), and that in (6) changes to (10) and (11).

$$Z_{v,1d} = (R_{v,1} + j\omega L_{v,1})[\cos(1.5T_s\omega) + j\sin(1.5T_s\omega)] \quad (8)$$

$$\begin{aligned} \text{Re}\{Z_{v,1d}\} &= R_{v,1} \cos(1.5T_s\omega) - \omega L_{v,1} \sin(1.5T_s\omega) \\ \text{Im}\{Z_{v,1d}\} &= R_{v,1} \sin(1.5T_s\omega) + \omega L_{v,1} \cos(1.5T_s\omega) \end{aligned} \quad (9)$$

$$Z_{v,2d} = \left( \frac{L_{v,2}^2 \omega^2}{R_{v,2}} - j\omega L_{v,2} \right) [\cos(1.5T_s\omega) + j\sin(1.5T_s\omega)] \quad (10)$$

$$\begin{aligned} \text{Re}\{Z_{v,2d}\} &= \frac{L_{v,2}^2 \omega^2}{R_{v,2}} \cos(1.5T_s\omega) + \omega L_{v,2} \sin(1.5T_s\omega) \\ \text{Im}\{Z_{v,2d}\} &= \frac{L_{v,2}^2 \omega^2}{R_{v,2}} \sin(1.5T_s\omega) - \omega L_{v,2} \cos(1.5T_s\omega) \end{aligned} \quad (11)$$

From either (9) or (11), the observation noted is imaginary and real terms of the virtual impedance can both become negative after introducing the finite time delay. The negative imaginary term will tend to shift the actual  $LCL$  resonance frequency  $\omega_{res}$ , while the negative real term will add open-loop RHP poles to the current control loop. The latter causes the non-minimum-phase behavior, which should preferably be avoided if a fast dynamic response is demanded. Comparing the real terms in (9) and (11) also informs that the negative paralleled virtual inductance ( $-L_{v,2}$ ) in Fig. 4 (c) helps to lessen the likelihood of  $\text{Re}\{Z_{v,2d}\}$  in (11) being negative. It is thus an important feature furnished by the HPF-based grid current active damping, which has so far been overlooked by [15] and [16], even though the same HPF scheme has been tried.

With this understanding, the next immediate task is to identify the critical frequency  $\omega_v$ , above which  $\text{Re}\{Z_{v,2d}\}$  in (11) becomes negative. The task can be done by first replacing  $G_{ad}(s)$  in (3) with the HPF parameters  $k_{ad}$  and  $\omega_{ad}$ . The expression obtained is given in (12), which when equated to

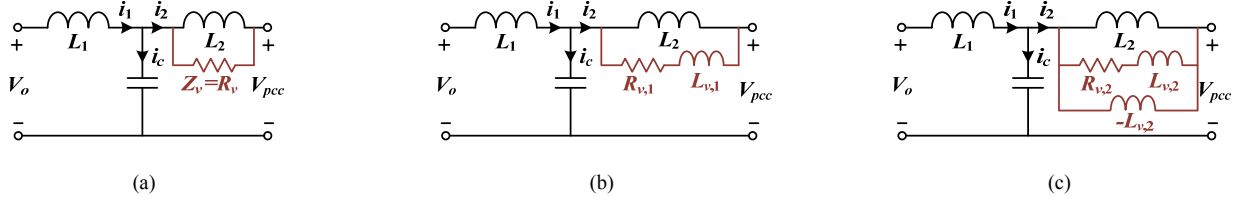


Fig. 4. Virtual impedance-based equivalent circuits realized by grid current active damping. (a) Single resistance. (b) Series  $RL$  damper. (c) Series  $RL$  damper with paralleled  $-L$ .

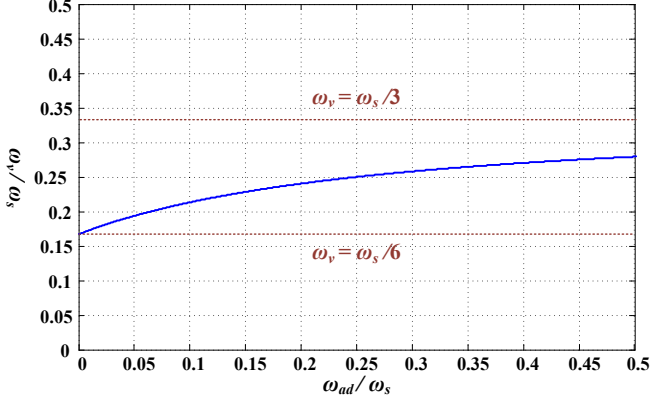


Fig. 5. Critical frequency  $\omega_v$  versus HPF cutoff frequency  $\omega_{ad}$ .

zero, leads to (13).

$$\text{Re}\{Z_{v,2d}\} = \frac{L_1 L_2 \omega^2}{k_{ad}} \cos(1.5T_s \omega) + \frac{L_1 L_2 \omega_{ad} \omega}{k_{ad}} \sin(1.5T_s \omega) \quad (12)$$

$$\text{Re}\{Z_{v,2d}\} = 0 \Rightarrow \frac{\omega_v}{\omega_s} \cos\left(\frac{3\pi\omega_v}{\omega_s}\right) + \frac{\omega_{ad}}{\omega_s} \sin\left(\frac{3\pi\omega_v}{\omega_s}\right) = 0 \quad (13)$$

where  $\omega_s = 2\pi f_s$  and  $f_s$  is the system sampling frequency.

Equation (13) can further be plotted as Fig. 5 for showing the relationship between critical frequency  $\omega_v$  and HPF cutoff frequency  $\omega_{ad}$ . It is shown in particular that with  $\omega_{ad} = 0$  or the HPF reduced to only a negative proportional gain ( $k_{ad} \neq 0$ ), the critical frequency read is  $\omega_v = \omega_s/6$ . This value can also be determined from the virtual impedance expression given in (3), which upon substituted with  $\omega_{ad} = 0$ , simplifies to (14). Any resonance frequency  $\omega_{res}$  above  $\omega_s/6$  considered for damping will then lead to negative  $\text{Re}\{Z_{v,2d}\}$ , and hence non-minimum-phase characteristic of the system. A simple solution is to invert the polarity of  $k_{ad}$  when  $\omega_{res} > \omega_s/6$  and  $\omega_{ad} = 0$ . Alternatively, active damping can be removed since it is not necessary for  $\omega_{res} > \omega_s/6$  [9], [12].

$$Z_{v,2d0} = \frac{L_1 L_2 \omega^2}{k_{ad}} [\cos(1.5T_s \omega) + j \sin(1.5T_s \omega)] \quad (14)$$

A third possibility is to set a non-zero  $\omega_{ad}$  for generating a high critical  $\omega_v$  that saturates at  $\omega_v = \omega_s/3$ . Damping of resonance in the range of  $\omega_s/6 \leq \omega_{res} \leq \omega_v < \omega_s/3$  can then be

performed with no negative virtual resistance introduced. Yet, above  $\omega_s/3$ , synthesis of negative virtual resistance cannot be avoided, which means the non-minimum-phase response will always be experienced. The value of  $\omega_s/3$  can therefore be referred to as the **theoretical** upper limit for  $\omega_v$  when a HPF with negated output is used for synthesizing the demanded active damping. This limit is, however, not achievable in practice, where noise amplification and digital sampling error will realistically limit the HPF cutoff frequency  $\omega_{ad}$  to below the Nyquist frequency of  $0.5\omega_s$ . With  $\omega_{ad} = 0.5\omega_s$  further assumed, Fig. 5 gives the companion **practical** upper limit as  $\omega_v \leq 0.28\omega_s$ , which needless to say, is smaller than the **theoretical** limit.

### III. DISCRETE Z-DOMAIN ANALYSIS

The impedance analyses in the  $s$ -domain aim to illustrate the active damping effects with the physical filter circuit, where components are always continuous. Therefore, demonstration of the circuit effects in the continuous  $s$ -domain is appropriate. Now, the intention is to co-design the discretized current controller and active damper, where classical control theory states that it is more accurately done in the  $z$ -domain. The root-locus analyses in this section are therefore performed in the  $z$ -domain, where results obtained can also be used for verifying the impedance-based equivalence identified earlier.

Parameters used for the analyses are given in Table I, where three different filter capacitance values have been included for generating three different  $LCL$  resonance frequencies. Alternatively, the different resonance frequencies can be obtained with different grid-side inductance  $L_2$  values, which certainly, can also be viewed as a change in grid inductance. Changing of capacitance is, however, preferred for the eventual experimental testing owing to the ease of obtaining well-tested commercial capacitors, whose values over a frequency range are available. Different capacitances, instead of inductances, have therefore been chosen for analysis without compromising the objective of obtaining different resonance frequencies.

#### A. Discrete $z$ -Domain Model

Fig. 6 illustrates the grid current control diagram in the discrete  $z$ -domain, where  $L_t$  has been used for combining  $L_2$  and  $L_g$  from Fig. 1 ( $L_t = L_2 + L_g$ ). A Zero-Order Hold (ZOH) block has also been included for modeling the Digital Pulse Width Modulation (DPWM) and its accompanied delay. The ZOH model is generally acceptable since it has been proven earlier to be a satisfactory approximation of the uniformly sampled DPWM, especially when its carrier is triangular [21], [22].

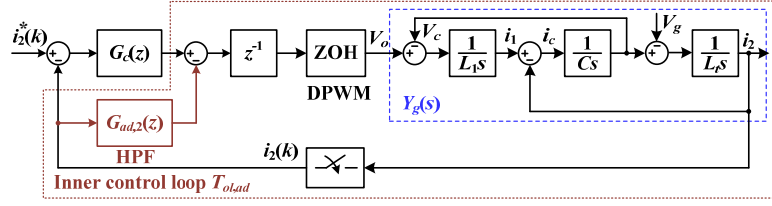


Fig. 6. Grid current control scheme in the  $z$ -domain.

Complementing the ZOH block is a  $z^{-1}$  delay block included for representing computational delay [20]. With these included blocks, transfer function  $Y_g(s)$  for representing the passive “plant” in Fig. 6 and (15) can eventually be discretized as (16), where  $H_{\text{ZOH}}(s)$  denotes the ZOH transfer function.

$$Y_g(s) = \frac{i_2}{V_o} \Big|_{V_g=0} = \frac{1}{L_1 L_t C_f s (s^2 + \omega_{\text{res}}^2)}, \quad \omega_{\text{res}} = \sqrt{\frac{L_1 + L_t}{L_1 L_t C}} \quad (15)$$

$$\begin{aligned} Y_g(z) &= Z[H_{\text{ZOH}}(s) \cdot Y_g(s)] \\ &= Z\left[\frac{1 - e^{-sT_s}}{s} \cdot \frac{1}{L_1 L_t C_f s (s^2 + \omega_{\text{res}}^2)}\right] \\ &= \frac{T_s}{(L_1 + L_t)(z - 1)} - \frac{(z - 1) \sin(\omega_{\text{res}} T_s)}{\omega_{\text{res}} (L_1 + L_t) [z^2 - 2z \cos(\omega_{\text{res}} T_s) + 1]} \end{aligned} \quad (16)$$

The PR controller  $G_c(s)$  in (1) and active damper  $G_{\text{ad},2}(s)$  in (7) can also be discretized by applying Tustin transformation with the former further pre-warped at the grid fundamental frequency [23]. The expressions obtained are given in (17) and (18).

$$G_c(z) = k_p + k_i \frac{\sin(\omega_1 T_s)}{2\omega_1} \frac{z^2 - 1}{z^2 - 2z \cos(\omega_1 T_s) + 1} \quad (17)$$

$$G_{\text{ad},2}(z) = \frac{2k_{\text{ad}}(1 - z)}{(\omega_{\text{ad}} T_s + 2)z + \omega_{\text{ad}} T_s - 2} \quad (18)$$

Using (16) to (18), the open-loop  $T_{ol}(z)$  and closed-loop  $T_{cl}(z)$  transfer functions for the grid current control scheme can neatly be derived as (19) and (20).

$$T_{ol}(z) = \frac{z^{-1} G_c(z) Y_g(z)}{1 + z^{-1} G_{\text{ad},2}(z) Y_g(z)} \quad (19)$$

$$T_{cl}(z) = \frac{z^{-1} G_c(z) Y_g(z)}{1 + z^{-1} [G_c(z) + G_{\text{ad},2}(z)] Y_g(z)} \quad (20)$$

### B. Effects of Negative Virtual Resistance

From Fig. 6, inclusion of  $G_{\text{ad},2}(z)$  can be viewed as the formation of an inner active damping control loop for reshaping

TABLE I  
MAIN CIRCUIT PARAMETERS

Symbol	Electrical Constant	Value
$V_g$	Grid voltage	400V
$f_1$	Grid frequency	50 Hz
$f_{\text{sw}}$	Switching frequency	10 kHz
$f_s$	Sampling frequency	10 kHz
$T_s$	Sampling period	100 $\mu$ s
$V_{\text{dc}}$	DC-link voltage	750 V
$L_1$	Converter-side filter inductor	1.8 mH
$L_2$	Grid-side filter inductor	1 mH
$C_f$	Filter capacitor	4.7/9.4/13.5 $\mu$ F
$L_g$	Grid inductance	0.8 mH

the  $LCL$  filter. Open-loop transfer function of this inner active damping loop can be written as (21), which will include unstable poles if negative virtual resistance is inserted by  $G_{\text{ad},2}(z)$ . These poles are related to the inner active damping loop only, excluding the outer PR controller. They appear as RHP poles, mentioned in Section II, when in the  $s$ -domain, and poles outside the unit circle when in the discrete  $z$ -domain. The initiation of negative virtual resistance can thus be sensed by identifying when the root loci of (21) move out of the unit circle in the  $z$ -domain.

$$T_{ol,ad}(z) = z^{-1} G_{\text{ad},2}(z) Y_g(z) \quad (21)$$

To illustrate, Fig. 7 shows the root loci of the inner damping loop obtained by closing the forward transfer function in (21) and changing  $k_{\text{ad}}$ . These root loci are also the open-loop pole trajectories of the outer grid current control loop. Presence of unstable poles in the inner damping loop will hence cause the outer grid current control loop to have non-minimum-phase behavior, as mentioned in Section II. For comparison, root loci for two different  $LCL$  resonance frequencies are considered with the first plotted in Fig. 7 (a) for  $\omega_{\text{res}} = 0.24\omega_s$  and  $C_f = 4.7 \mu\text{F}$ , and the second plotted in Fig. 7 (b) for  $\omega_{\text{res}} = 0.17\omega_s$  and  $C_f = 9.4 \mu\text{F}$ . For both plots, the HPF cutoff frequency  $\omega_{\text{ad}}$  is swept from 0 to  $0.5\omega_s$  (Nyquist frequency) with a step size of  $0.05\omega_s$ . The obtained root loci initially track outside the unit circle, but are gradually moved inside it as  $\omega_{\text{ad}}$  increases.

The inward shifting is, however, slower in Fig. 7 (a), whose root loci only enter the unit circle after  $\omega_{\text{ad}}$  crosses  $0.3\omega_s$ . The root loci in Fig. 7 (b), on the other hand, enter the unit circle upon  $\omega_{\text{ad}}$  rising above  $0.05\omega_s$ . These observations can be explained by noting that  $\omega_{\text{res}} = 0.24\omega_s$  in Fig. 7 (a), which according to Fig. 5, requires critical frequency  $\omega_v$  to be higher than  $0.24\omega_s$ . With a safety margin included,  $\omega_{\text{ad}}$  of the HPF



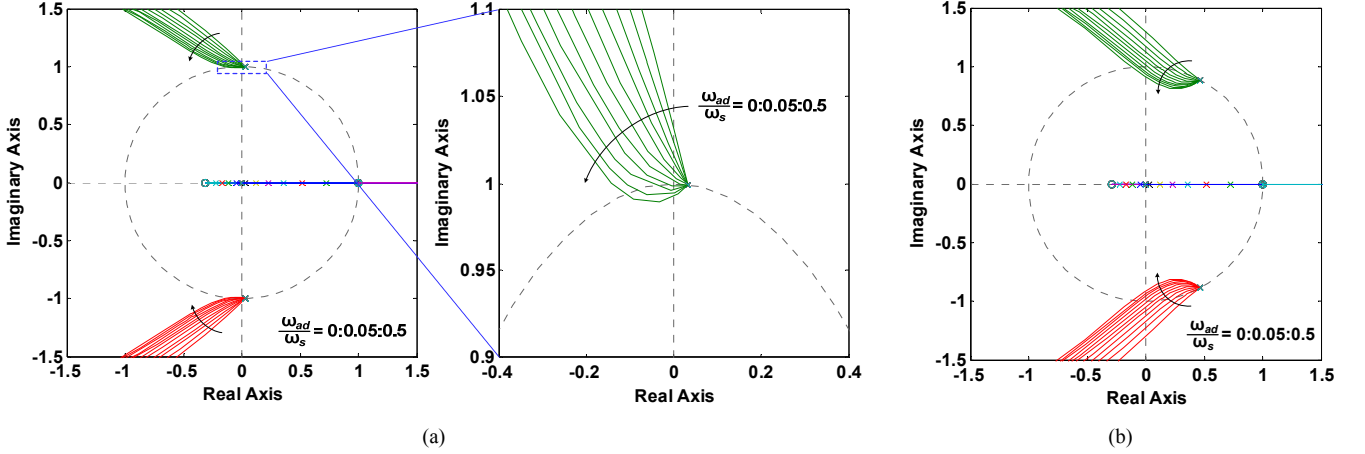


Fig. 7. Root loci of the active damping loop without the PR current controller. (a)  $C_f = 4.7 \mu\text{F}$ ,  $\omega_{res} = 0.24\omega_s$ . (b)  $C_f = 9.4 \mu\text{F}$ ,  $\omega_{res} = 0.17\omega_s$ .

should hence be chosen higher than  $0.3\omega_s$  according to Fig. 5. Similarly, with  $\omega_{res} = 0.17\omega_s$  in Fig. 7 (b),  $\omega_v$  must be higher than  $0.17\omega_s$ , which can be ensured by choosing  $\omega_{ad}$  higher than  $0.05\omega_s$  (with again a safety margin included). The discussed examples have therefore demonstrated the relevance of the impedance-based analyses presented in Section II, from which Fig. 5 has been derived for explaining phenomena observed in this subsection.

### C. Co-Design of Active Damper and Current Controller

The conventional approach towards designing an actively damped system is to design the grid current controller first followed by the active damper. For the former, plenty of existing references are available with [24] being an example. The method proposed in [24] uses only the total inductance ( $L_1 + L_t$ ) and a defined phase margin  $\theta_m$  for computing the parameters of (1), according to (22).

$$\omega_c = \frac{\pi - 2\theta_m}{3T_s}, \quad k_p = \omega_c(L_1 + L_t), \quad k_i = \frac{\omega_c}{10} \quad (22)$$

where  $\omega_c$  is the crossover frequency of the grid current control loop. Parameters of the PR grid current controller can then be included for designing the active damper based on root locus or other analytical techniques [8], [9], [15]. However, such a design procedure has overlooked the virtual impedance shaping effect that the active damping has introduced to the physical LCL filter. For grid current active damping, the introduced effect is shown in Fig. 4 (c) when a HPF with negative output is used as the damping transfer function (see (7)).

For illustrating more of the virtual impedance effects, Fig. 8 to Fig. 10 plot the closed-loop pole trajectories of the overall grid current control scheme with both proportional gain  $k_p$  of the PR current controller and active damping gain  $k_{ad}$  included. The former ( $k_p$ ) is continuously varied to obtain the root loci for a few chosen representative  $k_{ad}$  values. Moreover, since the resonant term of the PR controller is designed for obtaining the zero steady-state error at the fundamental frequency, its effect at the higher crossover frequency of the current control loop is comparably negligible. It is thus not included with the root

locus analyses [9].

The subsequent root locus plots obtained are for three different LCL resonance frequencies ( $\omega_{res} = 0.24\omega_s$ ,  $0.17\omega_s$ ,  $0.14\omega_s$ ), and for each plot (or resonance frequency), three cutoff frequencies ( $\omega_{ad} = 0.15\omega_s$ ,  $0.25\omega_s$ ,  $0.35\omega_s$ ) and four gains ( $k_{ad} = 0, 5, 15, 35$ ) of the HPF have been compared. Beginning with Fig. 8 for the case of  $\omega_{res} = 0.24\omega_s$  and  $C_f = 4.7 \mu\text{F}$ , the closed-loop poles can be kept within the unit circle even with  $k_{ad} = 0$  for representing no added active damping. Obtaining stable poles with  $k_{ad} = 0$  is, however, possible only when  $\omega_{res} > \omega_s/6$ , above which the system transport delay will create an inherent damping effect [9], [12]. Therefore, for Fig. 8, external active damping is strictly not necessary, but can be introduced for improved robustness in case that parameter drift causes  $\omega_{res}$  to fall below  $\omega_s/6$ .

Addition of external damping by setting  $k_{ad} \neq 0$  then results in prominent change in the root loci with both changes in  $k_{ad}$  and  $\omega_{ad}$  causing the closed-loop poles to move inside the unit circle. Consequently, the dynamic performance of the overall system is altered, implying that the grid current controller cannot be designed without considering the virtual impedance shaping effect introduced by the active damper. It should also be noted that  $k_{ad}$  cannot be increased excessively since it forces the root loci to move out of the unit circle from the right. This can be seen in Fig. 8 (a), where the right root paths are always out of the unit circle when  $k_{ad} = 35$ . The overall system is, therefore, always unstable regardless of how the grid current controller is designed. The “always unstable” upper limit of  $k_{ad}$  in Fig. 8 is also noted to increase with  $\omega_{ad}$  like demonstrated by the higher  $\omega_{ad} = 0.25\omega_s$  in Fig. 8 (b) and  $\omega_{ad} = 0.35\omega_s$  in Fig. 8 (c). The higher  $\omega_{ad}$  in either of the diagrams causes critical frequency  $\omega_v$  read from Fig. 5 to become higher than  $\omega_{res} = 0.24\omega_s$  set for Fig. 8. The non-minimum-phase behavior is, therefore, avoided when in Fig. 8 (b) and (c), permitting higher gains like  $k_{ad}$  in the active damper and  $k_p$  in the PR grid current controller to be used without causing instability.

The same root loci have been re-plotted in Fig. 9 and Fig. 10, but with lower resonance frequencies of  $\omega_{res} = 0.17\omega_s \approx \omega_s/6$  and  $\omega_{res} = 0.14\omega_s < \omega_s/6$  considered. Since  $\omega_{res}$  is no longer higher than  $\omega_s/6$ , inherent damping introduced by the transport



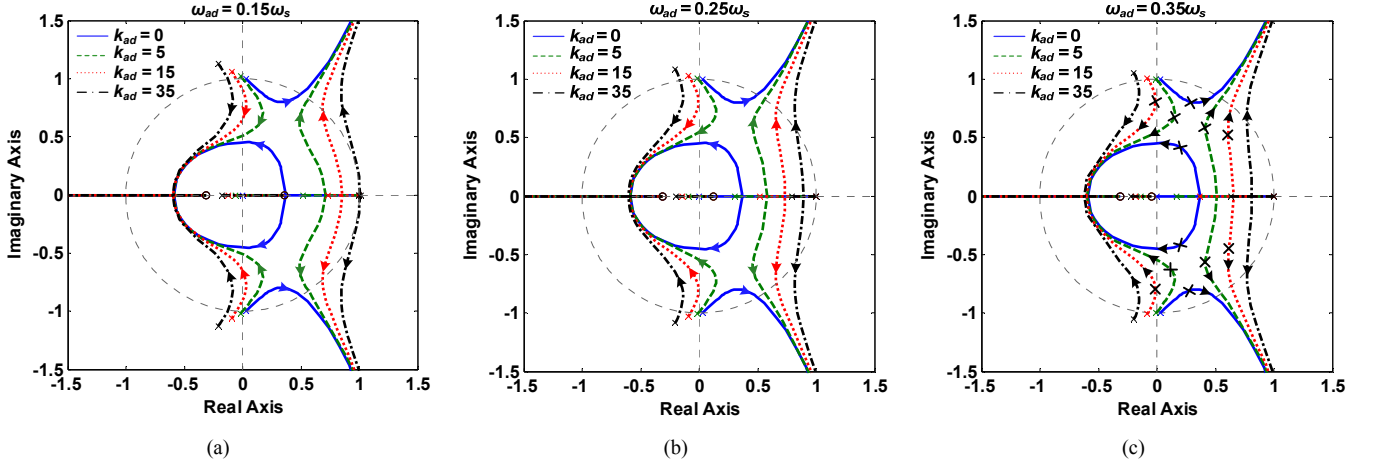


Fig. 8. Root loci of the grid current control loop with  $C_f = 4.7 \mu\text{F}$  and  $\omega_{res} = 0.24\omega_s$ . (a)  $\omega_{ad} = 0.15\omega_s$ . (b)  $\omega_{ad} = 0.25\omega_s$ . (c)  $\omega_{ad} = 0.35\omega_s$ .

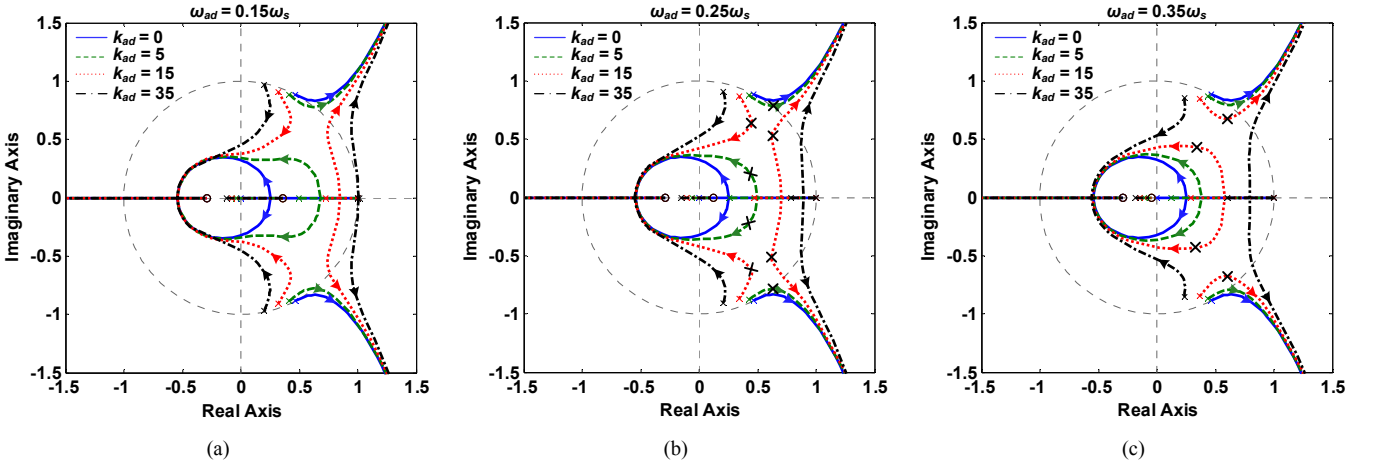


Fig. 9. Root loci of the grid current control loop with  $C_f = 9.4 \mu\text{F}$  and  $\omega_{res} = 0.17\omega_s$ . (a)  $\omega_{ad} = 0.15\omega_s$ . (b)  $\omega_{ad} = 0.25\omega_s$ . (c)  $\omega_{ad} = 0.35\omega_s$ .

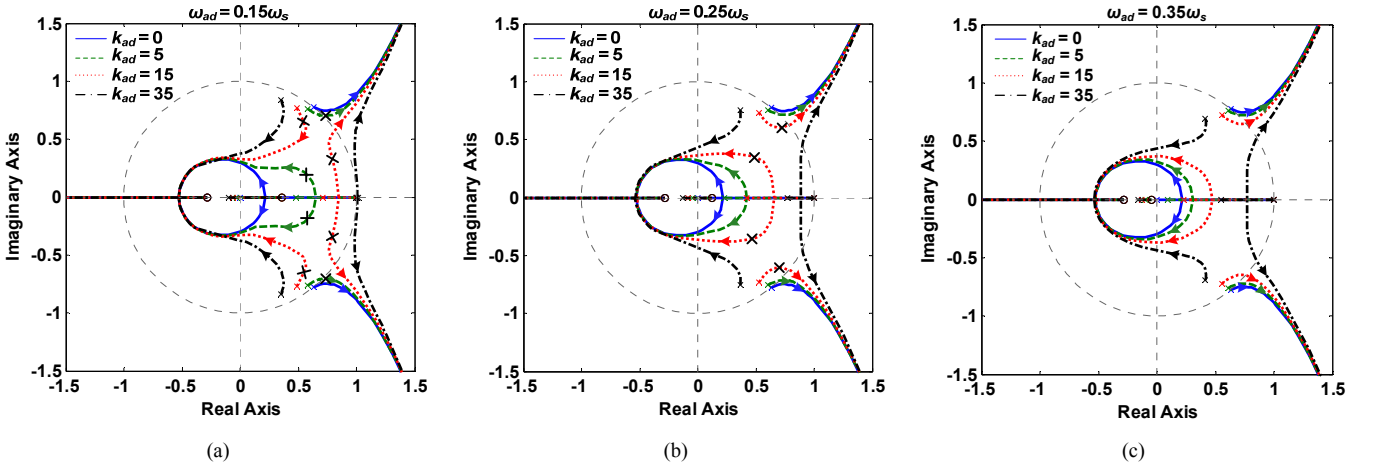


Fig. 10. Root loci of the grid current control loop with  $C_f = 14.1 \mu\text{F}$  and  $\omega_{res} = 0.14\omega_s$ . (a)  $\omega_{ad} = 0.15\omega_s$ . (b)  $\omega_{ad} = 0.25\omega_s$ . (c)  $\omega_{ad} = 0.35\omega_s$ .

delay is no longer applicable, causing the closed-loop poles to track outside the unit circle when  $k_{ad} = 0$ . Active damping is, therefore, necessary when in Fig. 9 and Fig. 10, unlike in Fig. 8.

Other than this, patterns of the root loci in Fig. 9 and Fig. 10 are also noted to be different, except for an observation related to  $k_{ad}$  which remains unchanged. More specifically, increase of

$k_{ad}$  is again noted to gradually destabilize the system with the root loci always located outside the unit circle on the right when  $k_{ad} = 35$  (see Fig. 9 (a) and Fig. 10 (a)). This upper limit of  $k_{ad}$  can similarly be raised by increasing  $\omega_{ad}$ , which unfortunately, is not always effective now. Explanation for that can be deduced from Fig. 9 (c), Fig. 10 (b) and (c), where it can be seen

that root loci related to  $k_{ad} = 15$  change their trajectories prominently as  $\omega_{ad}$  increases. A higher  $\omega_{ad}$  forces the root loci for  $k_{ad} = 15$  to move closer to the boundary of the unit circle rather than away from it. That gives lesser damping, which is certainly undesirable.

Parametric influences of the active damper on the system response must therefore not be ignored, and it is certainly not appropriate to design the grid current controller with only the total inductance considered, like in (22). An acceptable design for the overall control scheme can only be guaranteed when both HPF and current controller are co-designed simultaneously using root locus or other analytical techniques. In this section, root loci have been plotted in Fig. 8 to Fig. 10, where it has been shown that for each pair of given  $k_{ad}$  and  $\omega_{ad}$ , its accompanied root locus is formed by two conjugate pole trajectories moved along by two complex pole pairs. The pole pairs move in opposite directions as  $k_p$  increases. It is hence not straightforward to decide on the eventual set of parameters.

To resolve the problem, [25] uses a basic rule related to direct pole placement, which is to constrain all poles to have the same natural frequency. In other words,  $k_{ad}$ ,  $\omega_{ad}$ , and  $k_p$  should be co-designed such that the two conjugate pole trajectories intersect, and hence reducing the poles to only one conjugate pole pair. The conjugate pole pair must then be shifted so that it has the same natural frequency as the real pole. Such a design is, however, too restrictive. A slightly relaxed criterion is thus adopted for the design procedure recommended below, while still relying on direct pole placement in the  $z$ -domain for producing acceptable performance.

- 1) Identify the resonance frequency  $\omega_{res}$ , and then choose a few possible values for the HPF cutoff frequency  $\omega_{ad}$  from Fig. 5 that will help to avoid non-minimum-phase characteristic by ensuring that  $\omega_v > \omega_{res}$ .
- 2) Root loci like in Fig. 8 to Fig. 10 can be plotted using the chosen  $\omega_{ad}$  and  $k_{ad}$  values for studying their influences on the system closed-loop poles. A final value can then be decided for  $\omega_{ad}$  and another for  $k_{ad}$  through minimizing the distance between the two conjugate pole trajectories.
- 3) Two conjugate pole pairs with the shortest separation distance can then be marked, from which proportional gain  $k_p$  of the PR current controller can be determined. Natural frequencies of the conjugate pole pairs will then be the closest possible.
- 4) Since the resonant term of the PR controller has an effect only at the grid fundamental frequency, its resonant gain  $k_i$  can be approximately computed using (22) and an assumed crossover frequency  $\omega_c$  obtained by substituting phase margin  $\theta_m = 40^\circ$  to the first equation in (22). However, note that (22) is derived in [21] for a converter with  $L$ -filter only. It is therefore only an approximation, where  $\omega_c$  does not give the actual crossover frequency of the  $LCL$ -filtered system.
- 5) The procedure can be iterated, where necessary.

#### IV. EXPERIMENTAL RESULTS

For verification, the three-phase converter and  $LCL$  filter shown in Fig. 1 were implemented and connected to a California Instruments MX-series AC power supply for emulating the grid. Circuit parameters used for the setup are listed in Table I, while Table II lists parameters of the PR controller and active damper designed using Fig. 8 to Fig. 10. Corresponding closed-loop poles obtained using Table II are also marked with “X” in the figures. The designed control scheme was eventually implemented using a dSPACE DS1006 platform with a DS5101 digital waveform output board for generating the modulating pulses. Additionally, a DS2004 high-speed analog-to-digital board was used for sampling the PCC voltage and grid current values in synchronism with the modulating pulses.

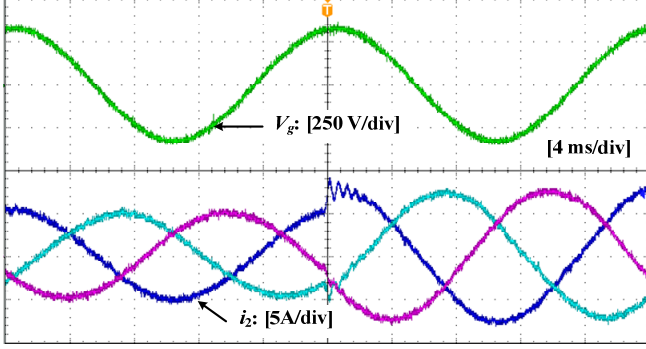
With the implemented setup, Fig. 11 shows its measured grid voltage and current waveforms when  $\omega_{res} = 0.24\omega_s$  and  $C_f = 4.7 \mu\text{F}$ . Since  $\omega_{res} > \omega_s/6$ , the system remains stable even with no active damping added, as demonstrated by Fig. 11 (a) with  $k_{ad} = 0$ . The system dynamic can however be improved by active damping, as understood from Fig. 8 (b) and (c). Corresponding results for showing the improved dynamic are given in Fig. 11 (b) for  $k_{ad} = 5$  and Fig. 11 (c) for  $k_{ad} = 15$ . Both figures use the same  $\omega_{ad} = 0.35\omega_s$ , and experience the same current step from 5 A to 7.5 A. Compared with Fig. 11 (a), Fig. 11 (b) and (c) exhibit faster response with shorter settling time and improved damping. These figures also confirm that with  $\omega_{ad} = 0.35\omega_s$ ,  $\omega_{res}$  is lower than the critical frequency of  $\omega_v = 0.27\omega_s$  read from Fig. 5. The improved damping in Fig. 11 (b) and (c) is therefore related to the positive virtual resistance inserted when  $\omega_{res} < \omega_v$ . A slightly improved transient response can also be seen from Fig. 11 (b) when compared with Fig. 11 (c). This observation is in agreement with the pole locations marked in Fig. 8 (c).

Fig. 12 next shows the grid voltage and current waveforms when the filter resonance frequency was changed to  $\omega_{res} = 0.17\omega_s \approx \omega_s/6$  by using  $C_f = 9.4 \mu\text{F}$ . Since  $\omega_{res}$  is no longer higher than  $\omega_s/6$ , the system cannot be stabilized without active damping, as demonstrated by Fig. 12 (a) obtained with a small  $k_{ad}$  of 5,  $\omega_{ad} = 0.25\omega_s$ . It shows a critically stable operation, which matches with the dash-lined root locus in Fig. 9 (b). Note that  $k_{ad}$  has not been reduced further since it caused high oscillatory current that tripped the system over-current protection during the testing. Results for an increased  $k_{ad}$  of 15, but the same  $\omega_{ad}$ , are provided in Fig. 12 (b). It can be seen from the results that the system is effectively damped by the larger  $k_{ad}$ , which hence confirms the dotted root locus drawn in Fig. 9 (b).

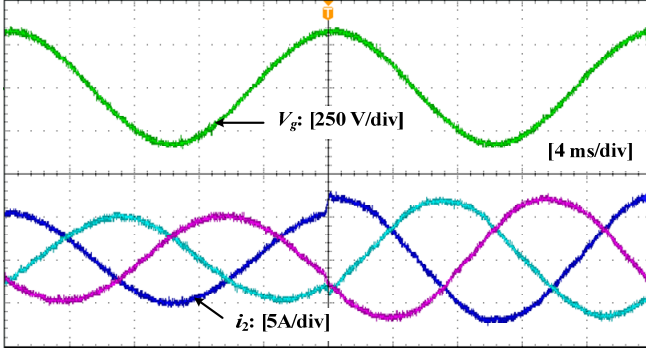
For both Fig. 12 (a) and (b), it should also be mentioned that the system does not exhibit the non-minimum-phase behavior, because  $\omega_{res}$  is below  $\omega_v = 0.25\omega_s$  read from Fig. 5 when  $\omega_{ad} = 0.25\omega_s$ . The non-minimum-phase behavior will be avoided too when  $\omega_{ad}$  is increased to  $0.35\omega_s$ . However, according to Fig. 9 (c) plotted with  $\omega_{ad} = 0.35\omega_s$ , root locus corresponding to  $k_{ad} = 15$  is shown to shift closer to the unit circle. The system is thus comparably less damped. This expectation has been verified by

TABLE II  
CONTROLLER PARAMETERS

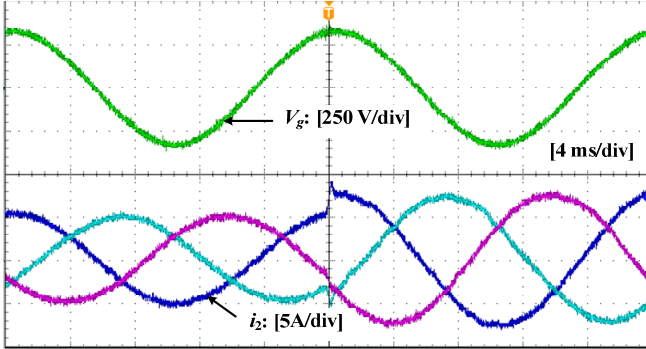
Test Case	PR Controller ( $k_p$ )	PR Controller ( $k_i$ )	HPF ( $\omega_{ad}$ )	HPF ( $k_{ad}$ )
Case I $C_f = 4.7 \mu\text{F}$ , $\omega_{res} = 0.24\omega_s$	16	600	$0.35\omega_s$	0/5/15
Case II $C_f = 9.4 \mu\text{F}$ , $\omega_{res} = 0.17\omega_s$	12	600	$0.25\omega_s/0.35\omega_s$	5/15
Case III $C_f = 14.1 \mu\text{F}$ , $\omega_{res} = 0.14\omega_s$	9	600	$0.15\omega_s/0.25\omega_s$	5/15



(a)

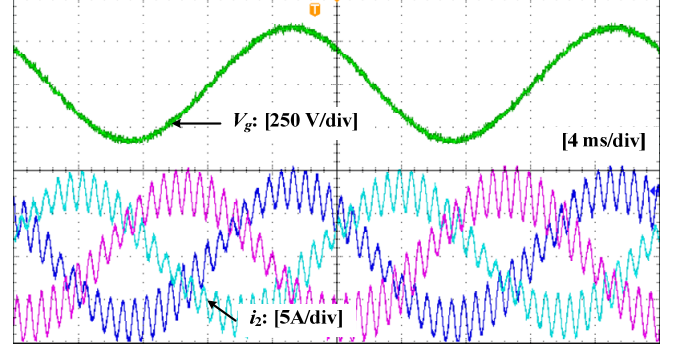


(b)

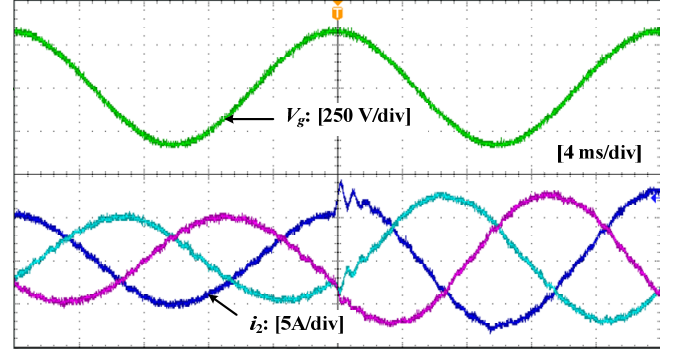


(c)

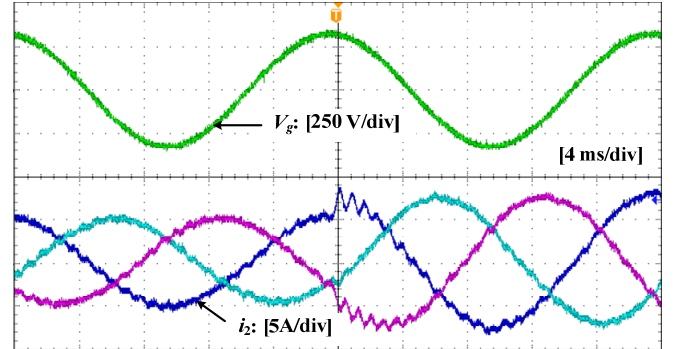
Fig. 11. Measured grid voltage and currents when  $\omega_{res} = 0.24\omega_s$  and  $C_f = 4.7 \mu\text{F}$ . (a)  $k_{ad} = 0$ . (b)  $k_{ad} = 5$ ,  $\omega_{ad} = 0.35\omega_s$ . (c)  $k_{ad} = 15$ ,  $\omega_{ad} = 0.35\omega_s$ .



(a)



(b)



(c)

Fig. 12. Measured grid voltage and currents when  $\omega_{res} = 0.17\omega_s$  and  $C_f = 9.4 \mu\text{F}$ . (a)  $k_{ad} = 5$ ,  $\omega_{ad} = 0.25\omega_s$ . (b)  $k_{ad} = 15$ ,  $\omega_{ad} = 0.25\omega_s$ . (c)  $k_{ad} = 15$ ,  $\omega_{ad} = 0.35\omega_s$ .

the more oscillatory transient grid current waveforms observed in Fig. 12 (c) when compared with those in Fig. 12 (b).

Comparing Fig. 12 (c) with Fig. 11 (c), another important observation should be noted too. Both figures are obtained with the same active damping parameters, but a decrease of the resonance from  $\omega_{res} = 0.24\omega_s$  in Fig. 11 (c) to  $0.17\omega_s$  in Fig. 12 (c) has significantly degraded the system transient performance even though a smaller proportional gain  $k_p$  (16 for Fig. 11 (c) in

comparison with 12 for Fig. 12 (c)) has been used with the grid current controller. Indirectly, it implies that the active damper and current controller must be co-designed simultaneously since their parameters affect each other.

The same grid voltage and current waveforms are re-plotted in Fig. 13, but now for an even lower resonance frequency of  $\omega_{res} = 0.14\omega_s < \omega_s/6$  obtained with  $C_f = 14.1 \mu\text{F}$ . Since  $\omega_{res}$  is again lower than  $\omega_s/6$ , reducing  $k_{ad}$  to zero will gradually lead

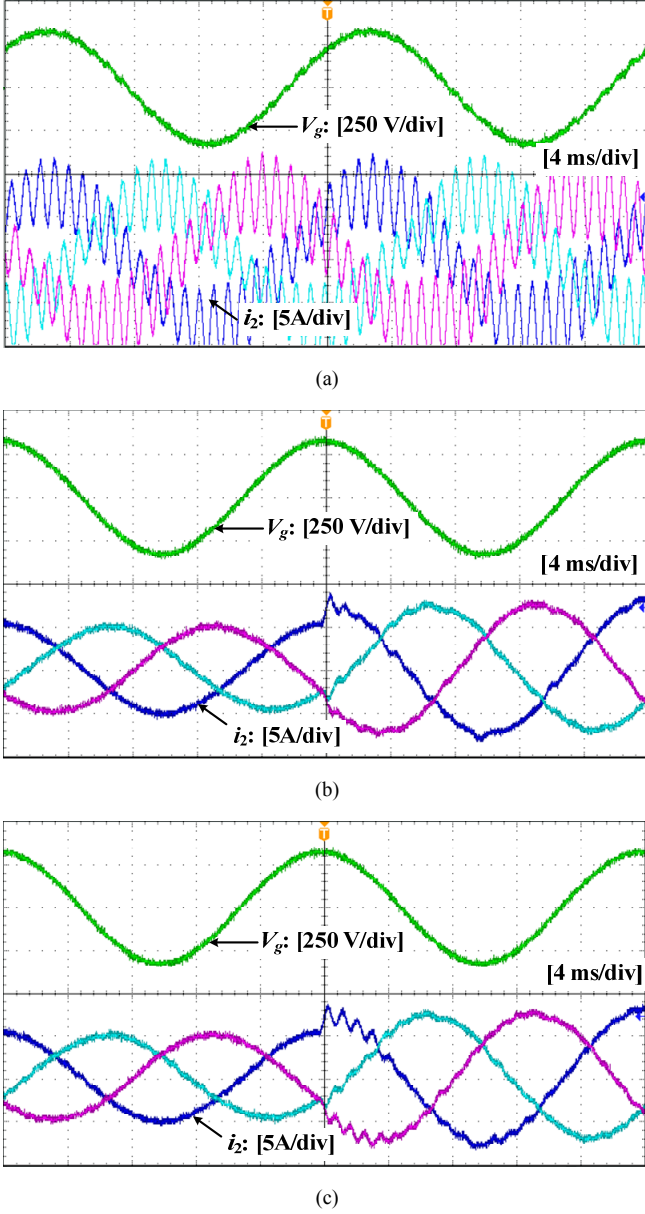


Fig. 13. Measured grid voltage and currents when  $\omega_{res} = 0.14\omega_s$  and  $C_f = 14.1 \mu\text{F}$ . (a)  $k_{ad} = 5$ ,  $\omega_{ad} = 0.15\omega_s$ . (b)  $k_{ad} = 15$ ,  $\omega_{ad} = 0.15\omega_s$ . (c)  $k_{ad} = 15$ ,  $\omega_{ad} = 0.25\omega_s$ .

to instability according to the dashed root locus plotted in Fig. 10 (a). This expectation has been confirmed by results shown in Fig. 13 (a) for  $k_{ad} = 5$  and  $\omega_{ad} = 0.15\omega_s$ . Also observed from Fig. 13 (b) and (c) for the same  $k_{ad} = 15$  is the more oscillatory transient response of the latter obtained with a higher  $\omega_{ad} = 0.25\omega_s$ . This observation has similarly been explained when analyzing root loci for the same  $k_{ad} = 15$  in Fig. 10 (a) and (b). Fig. 10 (b), in particular, uses a higher  $\omega_{ad} = 0.25\omega_s$ , whose effect is to push the root loci closer to the boundary of the unit circle. Expected dynamic response from Fig. 10 (b) will hence be more oscillatory or less damped, as verified by Fig. 13 (c) in comparison with Fig. 13 (b).

Further comparison between Fig. 13 (c) and Fig. 12 (b), which use the same active damping parameters, can also be performed, where the lower resonance at  $\omega_{res} = 0.14\omega_s$  has

caused the results in Fig. 13 (c) to be dynamically poorer even though a smaller proportional gain of  $k_p = 9$  has been used with it. This finding is similar to that concluded earlier when comparing Fig. 11 (c) and Fig. 12 (c). The preferred value for  $\omega_{ad}$  in Fig. 13 has lastly been noted to be lower than that in Fig. 12, which is, to a great extent, expected since the smaller  $\omega_{res}$  in Fig. 13 does not demand a high  $\omega_{ad}$  for mitigating the non-minimum-phase response caused by the unintentionally inserted negative virtual resistance (based on Fig. 5).

## V. CONCLUSIONS

This paper studies grid current active damping and control for *LCL*-filtered voltage source converters. Through systematic impedance-based analyses, it has been shown that active damping with grid current feedback is equivalent to adding a virtual impedance in parallel with the grid-side filter inductance. This virtual impedance has further been shown to be a series *RL* branch in parallel with a negative inductance when a HPF with negative output is used for implementing the active damper. The introduced negative inductance is particularly helpful for reducing non-minimum-phase behavior caused by transport delays in a digital system. Parametric influences of the active damper and current controller have also been studied through root locus analyses, where it has been shown that parameters of the active damper influence the system poles greatly. They have therefore been included in the co-design procedure recommended for the active damper and grid current controller. Experimental results obtained have shown the anticipated steady-state and transient performances, hence validating concepts presented in the paper.

## REFERENCES

- [1] M. Liserre, F. Blaabjerg, and S. Hansen, "Design and control of an *LCL*-filter-based three-phase active rectifiers," *IEEE Trans. Ind. Appl.*, vol. 41, no. 5, pp. 1281-1291, Sept./Oct. 2005.
- [2] R. N. Beres, X. Wang, F. Blaabjerg, C. L. Bak, and M. Liserre, "A review of passive filters for grid-connected voltage source converters," in *Proc. IEEE APEC* 2014, pp. 2208-2215.
- [3] J. Dannehl, M. Liserre and F. Fuchs, "Filter-based active damping of voltage source converters with *LCL* filter," *IEEE Trans. Ind. Electron.*, vol. 58, no. 8, pp. 3623-3633, Aug. 2011.
- [4] J. Dannehl, F. W. Fuchs, S. Hansen, and P. Thogersen, "Investigation of active damping approaches for PI-based current control of grid-connected pulse width modulation converters with *LCL* filters," *IEEE Trans. Ind. Appl.*, vol. 46, no. 4, pp. 1509-1517, Jul./Aug. 2010.
- [5] V. Blasko and V. Kaura, "A novel control to actively damp resonance in input LC filter of a three-phase voltage source converter," *IEEE Trans. Ind. Appl.*, vol. 33, no. 2, pp. 542-550, Mar./Apr. 1997.
- [6] V. Miskovic, V. Blasko, T. Jahns, A. Smith, and C. Romenesko, "Observer based active damping of *LCL* resonance in grid connected voltage source converters," in *Proc. IEEE ECCE* 2013, pp. 4850-4856.
- [7] D. Pan, X. Ruan, C. Bao, W. Li, and X. Wang, "Capacitor-current-feedback active damping with reduced computation delay for improving robustness of *LCL*-type grid-connected inverter," *IEEE Trans. Power Electron.*, vol. 29, no. 7, pp. 3414-3427, Jul. 2014.
- [8] X. Wang, F. Blaabjerg, and P. C. Loh, "Design-oriented analysis of resonance damping and harmonic compensation for *LCL*-filtered voltage source converters," in *Proc. IEEE IPEC* 2014, pp. 216-223.
- [9] S. G. Parker, B. P. McGrath, and D. G. Holmes, "Regions of active damping control for *LCL* filters," *IEEE Trans. Ind. Appl.*, vol. 50, no. 1, pp. 424-432, Jan./Feb. 2014.
- [10] J. Dannehl, C. Wessels, and F. W. Fuchs, "Limitations of voltage-oriented PI current control of grid-connected PWM rectifiers with *LCL* filters," *IEEE Trans. Ind. Electron.*, vol. 56, no. 2, pp. 380-388, Feb. 2009.

- [11] R. Teodorescu, F. Blaabjerg, M. Liserre, and A. Dell'Aquila, "A stable three-phase LCL-filter based active rectifier without damping," in *Proc. IAS* 2003, pp. 1552-1557.
- [12] J. Yin, S. Duan, and B. Liu, "Stability analysis of grid-connected inverter with LCL filter adopting a digital single-loop controller with inherent damping characteristic," *IEEE Trans. Ind. Inform.*, vol. 9, no. 2, pp. 1104-1112, May 2013.
- [13] X. Wang, F. Blaabjerg, and W. Wu, "Modeling and analysis of harmonic stability in an AC power-electronics-based power system," *IEEE Trans. Power Electron.*, vol. PP, no. 99, pp. 1-12, Feb. 2014.
- [14] C. Dick, S. Richter, M. Rosekit, J. Rolink, and R. De Doncker, "Active damping of LCL resonance with minimum sensor effort by means of a digital infinite impulse response filter," *Proc. EPE* 2007, pp. 1-8.
- [15] M. Hanif, V. Khadkikar, W. Xiao, and J. L. Kirtley, "Two degrees of freedom active damping technique for LCL filter based grid connected PV systems," *IEEE Trans. Ind. Electron.*, vol. 61, no. 6, pp. 2795-2803, Jun. 2014.
- [16] J. Xu, S. Xie and T. Tang, "Active damping-based control for grid-connected LCL-filtered inverter with injected grid current feedback only," *IEEE Trans. Ind. Electron.*, vol. 61, no. 9, pp. 4746-4758, Sept. 2014.
- [17] B. Bahrani, M. Vasiladiotis, and A. Rufer, "High-order vector control of grid-connected voltage-source converters with LCL-filters," *IEEE Trans. Ind. Electron.*, vol. 61, no. 6, pp. 2767-2775, Jun. 2014.
- [18] S. Chung, "A phase tracking system for three phase utility interface inverters," *IEEE Trans. Power Electron.*, vol. 15, no. 3, pp. 431-438, May 2000.
- [19] T. Messo, J. Jokipii, A. Mäkinen, T. Suntio, "Modeling the grid synchronization induced negative-resistor-like behavior in the output impedance of a three-phase photovoltaic inverter," in *Proc. IEEE PEDG* 2013, pp.1-8.
- [20] S. Buso and P. Mattavelli, *Digital Control in Power Electronics*, San Francisco, CA: Morgan & Claypool Publ., 2006.
- [21] D. M. Van de Sype, K. D. Gusseme, A. P. Van den Bossche, and J. A. Melkebeek, "Small-signal Laplace-domain analysis of uniformly-sampled pulse-width modulators," in *Proc. IEEE PESC* 2004, pp. 4292-4298.
- [22] D. M. Van de Sype, K. D. Gusseme, F. D. Belie, A. P. Van den Bossche, and J. A. Melkebeek, "Small-signal z-domain analysis of digitally controlled converters," *IEEE Trans. Power Electron.* vol. 21, no. 2, pp. 470-478, Mar. 2006.
- [23] A. G. Yepes, F. Freijedo, O. Lopez, and J. Gandoy, "High-performance digital resonant controllers implemented with two integrators," *IEEE Trans. Power Electron.*, vol. 26, no. 2, pp. 563-576, Feb. 2011.
- [24] D. G. Holmes, T. A. Lipo, B. P. McGrath, and W. Y. Kong, "Optimized design of stationary frame three phase AC current regulators," *IEEE Trans. Power Electron.*, vol. 24, no. 11, pp. 2417-2426, Nov. 2009.
- [25] R. Turner, S. Walton, and R. Duke, "Robust high-performance inverter control using discrete direct-design pole placement," *IEEE Trans. Ind. Electron.* vol. 58, no. 1, pp. 348-357, Jan. 2011.